COMPARISON OF MICROSAC AND VCO DIESEL INJECTOR NOZZLES IN TERMS OF INTERNAL NOZZLE FLOW CHARACTERISTICS.

Salvador, FJ[1] (*), Carreres, M.[1], Jaramillo, D.[1], Martínez-López, J.[2]

[1]CMT-Motores Térmicos, Universitat Politècnica de València

Camino de Vera s/n, E-46022 Spain.

[2] Koenigsegg Automotive AB

262 74 Ängelholm

Sweden

(*) Corresponding author:

Dr. F. J. Salvador, fsalvado@mot.upv.es

CMT-Motores Térmicos, Universitat Politècnica de València

Camino de Vera s/n, E-46022 Spain.

Telephone: +34-963879659

FAX: +34-963877659

ABSTRACT

A computational study focused on the inner nozzle flow and cavitation phenomena has been reported in this paper in order to investigate the two most common types of diesel injector nozzles at the present: microsac and valve covered orifice (VCO). The geometrical differences among both types of nozzles are mainly located at the needle seat, upstream of the discharge orifices. In the case of microsac nozzles there is a small volume upstream of the discharge orifices which is not present in VCO nozzles. Due to these geometrical differences among both type of nozzles, differences in the inner flow and the cavitation development have been found and analysed in this research. For the study, two cylindrical nozzles with six orifices and the same outlet diameter have been experimentally characterized in terms of mass flow rate. These measurements have been used to validate the CFD results obtained with the code OpenFOAM used for the analysis of the internal nozzle flow. For the simulations, two meshes that reproduce the microsac and VCO nozzles seat geometry while keeping the same geometry at the orifices have been built. The simulations have been carried out with a code previously validated and able to simulate cavitation phenomena using a homogeneous equilibrium model (HEM) and with RANS approach for the turbulence modelling (RNG k-ε).

For the computational study, three injection pressures and different geometries simulating different needle lifts have been used. The comparison among nozzles has been made in terms of mass flow, momentum flux and effective velocity and in terms of other non-dimensional parameters which are useful for describing the inner nozzle flow: discharge coefficient (C_d), area coefficient (C_a) and velocity coefficient (C_v). The analysis performed by studying and comparing the particularities of the flow in each nozzle has been useful in order to explain the experimental differences found in terms of mass flow rate and critical cavitation conditions.

One of the main conclusions of this study is the higher influence of the needle on the mass flow, momentum and injection velocity results for the VCO nozzle as compared to the microsac one. Hence, whereas in the first one these variables scale with the needle lift value, in the second one there is an intermediate needle lift from which they stop being influenced by the presence of the needle.

Furthermore, the study has also revealed important differences in the proneness to produce cavitation and its morphology. For the VCO nozzle, cavitation phenomenon occurs only in the upper part of the orifice inlet. However, for the microsac nozzle cavitation appears both at the upper and the lower part of the nozzle orifice entrance.

KEYWORDS

Nozzle, Diesel, Valve Covered Orifice (VCO), microsac, CFD, injection, cavitation.

LIST OF NOTATION

A_{eff} outlet effective area

A_o outlet area

C_a area coefficient

C_d discharge coefficient

C_v velocity coefficient

$C_{\varepsilon 1}$ constant for ε transport equation calculation

$C_{\varepsilon 2}^{o}$ variable for ε transport equation calculation

$C_{\varepsilon 2}$ constant for ε transport equation calculation

C_{μ} constant for turbulent viscosity calculation

c speed of sound

D_i diameter at the orifice inlet

D_o diameter at the orifice outlet

K cavitation number

k turbulent kinetic energy

L orifice length

$\dot{M}_f$ momentum flux

$\dot{m}_f$ mass flow

P pressure

P_b discharge back pressure

P_{in} injection pressure

P_{vap} vaporisation pressure

p_k production of turbulent kinetic energy

r rounding radius at the inlet orifice

t time

u velocity

$\bar{u}$ averaged velocity

u' fluctuating velocity

u_{eff} effective velocity

u_{th} theoretical velocity

S mean strain

S_{ij} strain tensor

GREEK SYMBOLS:

ΔP pressure drop, $\Delta P = P_{in} - P_b$

Ψ fluid compressibility

Ψ_l liquid compressibility

Ψ_v vapour compressibility

α_ε constant for ε transport equation calculation

α_k constant for *k* transport equation calculation

β constant for the turbulence model

γ vapour mass fraction

ε turbulence dissipation rate

μ fluid viscosity

μ_l liquid viscosity

μ_T turbulent viscosity

μ_v vapour viscosity

η expansion parameter

η_0 constant for the turbulence model

ρ fluid density

ρ_l liquid density

$\rho_{l,sat}$ liquid density at saturation

ρ_l^o liquid density at a given temperature condition

$\rho_{v,sat}$ vapour density at saturation

ρ_v vapour density

θ nozzle angle

1. INTRODUCTION

The study of modern Diesel engines is highly focused on the reduction of pollutant emissions like particulates and nitrogen oxides as well as fuel consumption, due to the new emission standards, global environmental awareness and fossil fuels prices ([1][2]). Both topics are related to the air-fuel mixing process and the subsequent combustion. The air-fuel mixing process depends on the injector characteristics and nozzle geometry ([3][4][5][6][7][8]) and the physical characteristics of fuel and air, which in turn depend on the pressure and temperature ([9][10]).

Among the different types of Diesel injectors nozzles that can be found in commercial use, the two most common ones are the microsac nozzles ([11][12][13][14]) and the VCO nozzles ([15][16][17][18]).

Other types like rotating nozzle [19], elliptical nozzles [20] and many others have been proposed, but in most cases they are only prototypes which are not in commercial use or their use is very scarce.

Some researchers have focused their studies on VCO nozzles ([15][16][17][18]). The internal nozzle flow characteristics of VCO nozzles [15], the sprays characteristics ([16][17]) and the combustion process [17] have been experimentally characterized in investigations reported in the literature. Internal nozzle flow and spray characteristics have also been studied computationally for this kind of nozzle [18]. The same type of studies have been conducted to study the particularities of the flow and the spray in the case of microsac nozzles ([11][12][13][14]).

Although there are some studies in the literature where microsac and VCO nozzles have been compared in terms of spray characteristics ([21][22]), computational studies on internal nozzle flow aiming at the investigation of the particularities of the flow in order to try to explain the differences observed experimentally have been not reported yet.

One of the broadest and most conclusive studies comparing the VCO and microsac nozzles experimentally was conducted by Bermúdez et al. ([21]). In this study, two nozzles with the same diameter with the only difference of its seat type were compared. The authors carried out mass flow rate, momentum flux and spray characterization measurements in non-evaporative conditions. The main conclusions of the comparison in stationary conditions with maximum needle lift were:

- The microsac nozzle exhibited a higher discharge coefficient.
- The microsac nozzle featured a higher effective injection velocity.
- The spray penetration was higher for the microsac nozzle, whereas the spreading angle was higher for the VCO nozzle.

Being a purely experimental study, the results could only be justified in an intuitive manner, attending to the differences existing in the nozzle part. However, these differences could not be verified nor a deeper study on them could be conducted, since a computational study was not carried out in parallel. The fact of working with nozzles with a high degree of convergence on their orifices and therefore non-cavitating [15] made it possible to compare both nozzles, decoupling the differences observed from the cavitation phenomena and attributing them exclusively to the geometrical differences among the nozzles. Thus, a study to determine the proneness of both kinds of nozzles to cavitate, as well as the differences in their cavitation structure and the consequences on the flow was not performed.

Considering the aforementioned conditions, the objective of this article is to compare both kinds of nozzles from the point of view of the behaviour of the inner flow, thus trying to explain the experimental evidences that were found in other studies in the literature and in the experimental tests carried out for the present study.

Both nozzles have the same orifice geometry, but they differ in the seat structure. Moreover, in order to perform a more complete analysis, nozzles with cylindrical orifices (thus prone to cavitate

[15][23]) have been used, so as to be able to study how cavitation affects the flow peculiarities in both geometries. With the aim of extending the comparison as far as possible, both nozzles have been compared using mesh geometries that simulate different needle lifts, since the flow particularities may be affected in a different way in both kinds of nozzle geometry due to the presence of the needle.

For this study, a Homogeneous Equilibrium Model (HEM) implemented in the version 1.5 of OpenFOAM® [24] and able to model the cavitation phenomenon was used. This code has been extensively validated against experimental data in terms of mass flow measurements, momentum flux measurements and injection velocity at the nozzle outlet reported in previous studies ([25][26][27]). The results obtained from simulations and their comparison with the experimental data showed that the model is able to accurately predict the behaviour of the fluid in both cavitating and non-cavitating conditions.

However, for both geometries to be analysed, injection rate measurements are performed, which allow yet again to validate the code results in terms of mass flow rate as a function of the pressure difference, as well as in terms of determining the cavitation critical conditions.

As far as the structure of the paper is concerned, it has been divided into 6 sections. First of all, the CFD approach will be briefly described (section 2) and validated for both nozzles at two different injection pressures with experimental steady mass flow rate at maximum needle lift (section 3). Following, in section 4, an extensive comparison between both nozzles at six different needle lifts in terms of mass flow, momentum flux, effective velocity, non-dimensional parameters and cavitation appearance will be presented. Finally, the main conclusions of the present investigation and the relationship with previous experimental findings reported in the literature will be drawn in section 5.

2. DESCRIPTION OF THE CFD APPROACH

2.1 Cavitation modelling.

As explained in [27], three approaches are mainly considered for modelling cavitation: two-phase flow models, interface tracking-capturing methods and continuum flow models (or one-fluid models). The first ones treat the liquid and vapour phases separately, solving a set of Navier-Stokes equations for each phase and linking them to mass and momentum transfer terms. Interface tracking and capturing methods assume the cavitating flow as two immiscible phases with different but constant densities, neglecting the viscous effects. For each phase, the model solves the continuity, momentum and energy equations, leaving the interface between both phases aside. The continuum flow models or homogeneous equilibrium models consider the liquid and vapour as a homogeneous mixture of two fluids behaving as one, making it unnecessary to solve the Navier-Stokes equations for each phase. The density of the fluid changes between the density of the pure liquid and pure vapour and it is calculated from an equation of state which generally relates pressure and density.

The code used in the present study for modelling cavitating flows is implemented in OpenFOAM ® [24]. This model, validated in calibrated orifices, one-hole and multi-hole nozzles by Salvador et al. in its laminar [25][26][27], turbulent RANS [14] and LES [28] versions belongs to the homogeneous equilibrium models (HEM), and therefore assumes the flow as a perfect mixture of liquid and vapour phases in each cell of the domain.

In HEM models, the assumptions of local kinematic equilibrium (local velocity is the same for both phases) and local thermodynamic equilibrium (temperature, pressure and free Gibbs enthalpy equality between phases) are made. This kind of model cannot reproduce strong thermodynamic or kinetic non-equilibrium effects, but it is often used for numerical simulations due to its simplicity and numerical stability. These two advantages are the main reasons why this model was chosen by the authors.

As stated before, the homogeneous equilibrium model calculates the growth of cavitation using a barotropic equation of state (Eq. (1)), which relates pressure and density through the compressibility of the mixture, being the compressibility the inverse of the speed of sound squared (Eq. (2)):

$$\left(\frac{\partial\rho\big(t,P(\vec{x},t)\big)}{\partial P}\right)_t = \Psi \tag{1}$$

$$\Psi = \frac{1}{c^2} \tag{2}$$

The amount of vapour in the fluid is calculated with the void fraction γ (Eq. (3)), which is 0 in a flow without cavitation and 1 for fully cavitating flows.

$$\gamma = max\left(min\left(\frac{\rho-\rho_{l,sat}}{\rho_{v,sat}-\rho_{l,sat}},1\right),0\right) \tag{3}$$

The compressibility of the mixture (Eq. (4)) is calculated from Ψ_v and Ψ_l (vapour and liquid compressibility, respectively) using a linear model. Although more accurate and complicated models can be found in the literature (Chung [29] and Stewart [30]), the linear model has been chosen due to its convergence and stability.

$$\Psi = \gamma\Psi_v + (1-\gamma)\Psi_l \tag{4}$$

In the case where there is only vapour or liquid, the following linear equation of state can be derived from Eq. (1) if the speed of sound is considered constant:

$$\rho_v = \Psi_v P \tag{5}$$

$$\rho_l = \rho_l^0 + \Psi_l P \tag{6}$$

The linear model has also been used to calculate the density and the viscosity of the mixture:

$$\rho = (1-\gamma)\rho_l^0 + \Psi P \tag{7}$$

$$\mu = \gamma\mu_v + (1-\gamma)\mu_l \tag{8}$$

The iteration process to numerically solve the fluid behaviour starts with the continuity equation (Eq. (9)) to get a provisional density.

$$\frac{\partial\rho}{\partial t} + \nabla\cdot(\rho\vec{u}) = 0 \tag{9}$$

According to previous studies performed by the authors [27], the divergence term $\nabla\cdot(\rho\vec{u})$is discretized in the space by using a Gauss upwind scheme to improve the stability, whereas an implicit discretisation in time is used for the density in the divergence term. With respect to the partial derivative over time, an Euler scheme is used for time discretisation. When the provisional density is computed, preliminary values for γ and Ψ are determined using Eqs. (3) and (4).

The next step is the calculation of a predictor for the velocity from the momentum conservation equation (Eq. (10)). The same procedure as before is followed: an Euler scheme for the partial derivatives over time and a Gauss upwind scheme for the divergence terms.

$$\frac{\partial(\rho\vec{u})}{\partial t} + \nabla \cdot (\rho\vec{u} \cdot \vec{u}) = -\nabla P + \nabla \cdot \left(\mu(\nabla\vec{u} + \nabla\vec{u}^T)\right) \tag{10}$$

Then the continuity equation (Eq. (9)) is modified with the equation of state (Eq. (7)) and the following equation is solved by an iterative PISO algorithm:

$$\frac{\partial(\Psi P)}{\partial t} - \left(\rho_l^0 + (\Psi_l - \Psi_v)P_{vap}\right)\frac{\partial}{\partial t} - P_{vap}\frac{\partial\Psi}{\partial t} + \nabla \cdot (\rho\vec{u}) = 0 \tag{11}$$

When the continuity convergence has been reached, the variables ρ, γ and Ψ are updated using Eqs. (7), (4) and (3), and the PISO algorithm is started again until convergence.

The convergence criteria used for all the simulations run in the present study is based on the local continuity and the residuals of all the flow variables. The local continuity is defined as the sum of all the cell flux imbalances and remains always below 1e-8 for all the needle lifts and pressure conditions simulated, which is a clear sign of the good convergence and stability of the code. The second criterion used to check the convergence of every simulation is the evolution of the residuals for each flow variable. The residuals are evaluated by substituting the current solution into the equation and taking the magnitude of the difference between the left and right hand sides and are forced to remain constant below 1e-8.

2.2 Turbulence modelling

The turbulence is modelled using a RANS (Reynolds-averaged Navier-Stokes) method. In the RANS methods the solution is split into an averaged solution and a fluctuating solution. In particular the RNG k-ε model [31] used for the present work uses the Boussinesq assumption to model the turbulent viscosity:

$$-\overline{u'_i u'_j} = \mu_t \left(\frac{\partial \overline{u_i}}{\partial x_j} + \frac{\partial \overline{u_j}}{\partial x_i} - \frac{2}{3} \frac{\partial \overline{u_k}}{\partial x_k} \delta_{ij} \right) - \frac{2}{3} k \rho \delta_{ij} \tag{12}$$

The eddy or turbulent viscosity is defined as:

$$\mu_t = \rho C_\mu \frac{k^2}{\varepsilon} \tag{13}$$

Where k and ε are the turbulent kinetic energy and the turbulence energy dissipation, respectively.

Two transport equations are associated with these variables:

$$\frac{\partial \rho k}{\partial t} + \nabla \cdot \left(\rho k \vec{\overline{u}} \right) = \nabla \cdot [(\mu + \mu_t \alpha_k) \nabla k] + p_k - \rho \varepsilon \tag{14}$$

$$\frac{\partial \rho \varepsilon}{\partial t} + \nabla \cdot \left(\rho \varepsilon \vec{\overline{u}} \right) = \nabla \cdot [(\mu + \mu_t \alpha_\varepsilon) \nabla \varepsilon] + C_{\varepsilon 1} \frac{\varepsilon}{k} p_k - C_{\varepsilon 2}^{o} \rho \frac{\varepsilon^2}{k} \tag{15}$$

With:

$$C_{\varepsilon 2}^{o} = C_{\varepsilon 2} + \frac{C_\mu \eta^3 \left(1 - \frac{\eta}{\eta_0} \right)}{1 + \beta \eta^3} \tag{16}$$

The new variables are the production of turbulent kinetic energy (p_k), expansion parameter (η) and the mean strain modulus(S), defined as:

$$p_k = \mu_t S^2 \tag{17}$$

$$\eta = \frac{Sk}{\varepsilon} \tag{18}$$

$$S = \sqrt{2 S_{ij} S_{ij}} \tag{19}$$

The coefficients used in the RNG k-ε model correspond to the values given by Yakhot et al. [31]:

$$C_{\varepsilon 1} = 1.42$$

$C_{\varepsilon 2} = 1.68$

$\alpha_k = 1.39$

$\alpha_\varepsilon = 1.39$

$C_\mu = 0.0845$

$\eta_0 = 4.38$

$\beta = 0.012$

3. NUMERICAL SIMULATIONS DESCRIPTION

3.1 Nozzles geometry.

The nozzles used for the study are cylindrical multi-hole nozzles with 6 orifices. In order to focus on the effect of the needle seat, the same geometrical characteristics of the orifices have been kept for both types of nozzles. In Table 1, the parameters defining the geometry of the orifices, such as the orifice length (*L*), rounding radius (*r*), diameter at the inlet (D_i), diameter at the orifice outlet (D_o) and nozzle angle (θ) are given. These parameters are geometrically defined in Fig. 1.

As mentioned before, the difference between both types of nozzles is mainly located at the needle seat: in the case of the VCO nozzle, when the nozzle is closed, the needle totally blocks the nozzle orifice. In the case of a microsac nozzle, even when the nozzle is totally closed, the orifice keeps connected with a small fuel reservoir in the nozzle sac. This situation can be observed in Fig. 1 considering the case of needle lift equal to 0.

Due to the symmetry of the geometry and from the point of view of the calculations, the nozzle has been reduced to only one of the holes (60º) in order to speed up the simulations. Two types of

Diesel injector nozzles at 6 different needle lifts ranging from 50μm to 250μm (full needle lift condition [21]) have been considered for the simulations for both the microsac nozzle and the VCO nozzle.

For the present investigation, the 12 geometries (2 nozzles and 6 needle lifts) have been discretised into hexahedral cells keeping a partially structured grid that follows the direction of the flow (improving the stability and convergence rate [32]) and a small transition zone just before the orifice inlet. Sensitivity studies of the mesh reported in previous studies ([27], [32]) made it possible to choose the most appropriate mesh refinements for the RANS calculations. As a result of those studies, it was established that the cell size in the hole should vary from around 7 μm in the orifice core to a minimum value of 1.15 μm near the wall region. For the rest of the cells at the nozzle, the cell size is fixed to 22.5 μm. With this cell size, the final mesh has around 200,000-240,000 cells. To perform the simulations, the supercomputer Tirant at the University of Valencia (Spain) [33] was used. It is formed by 256 IBM bladecenter JS20 on SUSE Linux Enterprise Server 10 and it has a computing power of 4.5 Tflops.

3.2 Boundary conditions and fluid properties.

The relevance of choosing a proper set-up for the boundary conditions to be able to ensure the convergence and the accuracy of the simulations is well-known. In the present study, as depicted in Fig. 2, a fixed pressure condition has been used at the inlet where the injection pressure is set, whereas a mean pressure condition has been established for the outlet (backpressure). The mean pressure condition keeps the mean desirable value, allowing zones with very low pressures as a result of the presence of vapour in the flow due to cavitation phenomenon. This boundary avoids the imposition of a rigorous pressure outlet that could affect the vapour structures developed as a consequence of the cavitation phenomenon [27]. A non-slip condition for the velocity has been used at the walls. Finally, symmetry conditions have been employed at the symmetry surfaces.

In order to extensively characterize and compare both nozzles in both cavitating and non-cavitating conditions, three representative injection pressures of actual engine running conditions have been considered: a low injection pressure (30 MPa), a medium injection pressure (80 MPa) and a high injection pressure (160 MPa). As far as the backpressure is concerned, seven different values have been simulated for the case of 30 MPa and nine different values for the case of 80 MPa. For the case of injection pressure of 160MPa, a more extensive range of backpressures has been chosen for the VCO nozzle in order to detect critical cavitation conditions with a total of 15 different values. For the microsac nozzle, 9 different values have been enough to characterize the critical cavitation conditions. All this information can be seen in Table 2. The aforementioned simulations pursued a double goal: on one hand, to characterize and compare both nozzles in a wide range of Reynolds numbers (from 6000 to 24000, approximately) and so, from a smaller to a higher degree of turbulence; on the other hand, to capture the injection conditions at which cavitation starts (critical cavitation conditions). Those conditions are expected to be different for each nozzle, and therefore the flow parameters describing the nature of the flow could behave in a different manner depending on the geometry.

With respect to the fluid properties introduced in the calculations, the density and viscosity values were taken from a commercial diesel fuel at 25ºC. The liquid compressibility was calculated from speed of sound measurements in diesel fuel [10] and the vapour properties have been obtained from a similar fuel from Kärrholm et al. [34].

3.3 Model validation.

As stated in the introduction, the code has been extensively validated using experimental measurements of standard nozzles based on measurements of mass flow and momentum flux ([14][25][26][27][28]). It is important to remark that momentum flux, apart from being one of the most important parameters that control the air-fuel mixing process in the spray ([35][36]), provide, in combination with mass flow measurements, important information such as effective injection velocity or effective injection area. The results of the numerical simulations were compared to the experimental data showing the ability of the model to predict the behaviour of the fluid in both cavitating and non-cavitating conditions with high level of reliability.

For the nozzles under study, again, a validation has been made by comparing the code results against experimental mass flow rate measurements. These tests were performed using an Injection Rate Discharge Curve Indicator (IRDCI) commercial system, which displays and records the data that describe the chronological sequence of an individual fuel injection event, with an uncertainty value of 1.5%. The methodology to carry out these measurements and theoretically derive the parameters describing the nozzle flow is thoroughly explained in [25]. Results are shown in Fig. 3, where the mass flow is represented as a function of the squared root of the pressure difference ($\sqrt{P_{in} - P_b}$). In the figure, the results for the injection pressure of 30 MPa are shown at the left side, whereas the right side corresponds to the injection pressure of 160 MPa. Each marker represents a different discharge pressure. In the case of 30 MPa, a mass flow linear increase is noticed as the squared root of the pressure difference increases up to a point (represented for each case with the letters CCC - critical cavitation conditions) from which the mass flow is collapsed and remains invariant even though the pressure difference is further increased. This behaviour has been observed in many occasions and it is, in fact, a non-intrusive manner of determining the critical cavitation conditions, that lead to the cavitation inception ([14][15][23][27]).

As far as the comparison among computational and experimental results is concerned, as it can be appreciated in the figure, the code is able to predict perfectly the trends and the changes in the flow behaviour due to cavitation. At low injection pressure, both experimental and computational values increase initially with the pressure difference and remain collapsed for the same backpressure values. For high injection pressure, the reliability of the code is even higher since it is able to predict the mass flow with a maximum deviation of 6%.

The comparison of results among the VCO and the microsac nozzle will be performed in a more exhaustive way in the following sections.

4. COMPUTATIONAL RESULTS AND ANALYSIS

Once the code is validated, a comparison of the results from both nozzles will be performed by analysing step by step the results obtained from the numerous computational cases simulated. First, the differences in the flow pattern when the injector works under stationary conditions of maximum needle lift (250 µm for the injector considered) are analysed. These conditions are representative of operating points of the engine at full load and once the injector opening transient stage is ended. Afterwards, results will be analysed for other 5 partial needle lifts, representative of what occurs during the injector opening and closing transient stages.

4.1 Analysis of Results at maximum needle lift.

4.1.1 Mass flow and cavitation phenomenon.

The results of mass flow ($\dot{m}_f$) at maximum needle lift for both nozzles and for the three injection pressures are depicted in the upper part of Fig. 4. These results are the same ones that were used for validation purposes in Fig. 3, but they have been completed with the results at medium injection pressure (80MPa). As can be seen, the mass flow is higher for the microsac nozzle for all the simulated conditions, although the differences between both nozzles decrease when increasing the backpressure (i.e. when moving to non cavitating conditions). As was stated before in the validation section, the mass flow increases linearly with the square root of pressure drop ($\sqrt{P_{in} - P_b}$) until it reaches a backpressure characterized by the beginning of the mass flow collapse usually called critical cavitation conditions (CCC). From this point, the mass flow remains unchanged regardless of the backpressure. This collapse is often used to detect cavitation experimentally ([14][15][23][27]). When a nozzle is more prone to cavitate, it starts cavitating for high values of backpressure (for a given injection pressure), which means lower values of ($\sqrt{P_{in} - P_b}$). For each injection pressure, the value of the backpressure that leads to cavitation inception is displayed in Table 3 for both nozzles.

The higher values of backpressure needed for the VCO nozzle to cavitate clearly indicate that this nozzle is more prone to cavitate than the microsac nozzle. This is mainly due to the higher deflection suffered by the streamlines in the upper corner of the orifice inlet in a VCO nozzle compared to a microsac nozzle according to the different topology of nozzles showed in Fig. 1. This explanation will be complemented in section 4.1.4 when differences found in cavitation structures will be addressed. The proneness to cavitation can be also analysed using the definition of cavitation number. There are several definitions for the cavitation number ([15][14][23]). One of them is the parameter K, defined as a function of injection pressure (P_{in}), the backpressure (P_b), and the vaporization pressure (P_{vap}) as Eq. (20) states. Given that the fuel vaporization pressure is much lower than the injection pressure, it is usual to disregard the term (P_{vap}) in the numerator:

$$K = \frac{P_{in} - P_{vap}}{P_{in} - P_b} \quad (20)$$

The way this parameter is defined, as the backpressure is reduced for a given injection pressure, the denominator grows larger and the numerator remains constant. This means that, the greater the pressure difference the nozzle is submitted to, the lower the value of K. The value of K related to the critical cavitation conditions is named as the critical cavitation number, K_{crit}. Attending to the critical discharge conditions depicted in Table 3, the value of K_{crit} of the studied nozzles is found among 1.44 and 1.46 for the VCO nozzle and between 1.29 and 1.3 for the microsac nozzle depending on the injection pressure. If the backpressure is further reduced once those conditions are reached, K takes lower values than the critical one, tending to the unity (thus reaching the maximum intensity of cavitation for the injection pressure level considered) when the backpressure tends to zero.

These results are totally consistent with the experimental evidences found by Bermúdez et al. [21] in comparative studies of VCO and microsac nozzles. As it was mentioned in the Introduction, Bermúdez et al. studied the mass flow and spray features for these two types of nozzles, which are identical to the ones simulated in the current paper. In the results analysis, higher discharge coefficients were found for the microsac nozzle, as it happens in the present study. In addition, the spreading angle proved to be higher for the VCO nozzle. This result, taking into account that one of the effects of cavitation is the increase of the spreading angle [15], is fully compatible with the higher level of cavitation found for the VCO nozzle for a certain injection pressure condition.

4.1.2 Momentum flux and effective velocity

In Fig. 4, below the results of mass flow rate already explained, the momentum flux ($\dot{M}_f$) for all the injection pressures and backpressures is depicted against the square root of pressure drop for both nozzles. As can be seen, momentum flux, which gives an idea of the impact force of the spray, increases with the squared root of pressure drop, $\sqrt{P_{in} - P_b}$, and as it was observed for the mass flow results, momentum flux is higher for the microsac nozzle as a result of lower friction losses in the channel feeding the orifices between the needle and internal nozzle wall. In contrast to the mass flow results, momentum flux does not show any collapse with cavitation development ([27] [28]).

With mass flow and momentum flux data, the effective injection velocity can be calculated by means of Eq. (21) and is defined as the theoretical velocity of the fuel considering that all the fluid is in the liquid phase flowing through an effective area smaller than the real outlet section (due to the presence of vapour bubbles) keeping the same mass flow and momentum flux values than in the real situation [25]. This effective velocity is also plotted as a function of the pressure drop in the bottom of Fig. 4.

$$u_{eff} = \frac{\dot{M}_f}{\dot{m}_f} \tag{21}$$

In the figure, an increase in the slope of the curve when cavitating conditions are reached can be appreciated. For instance, in the case of 30 MPa, according to Table 3, the backpressure for reaching cavitating conditions is around 7 MPa for the microsac nozzle and 9.5 MPa for the VCO nozzle. This means a value of $\sqrt{\Delta P}$ ≈4.8 MPa for the microsac and $\sqrt{\Delta P}$ ≈4.6 MPa for the VCO nozzle. For higher values of $\sqrt{\Delta P}$, the nozzles cavitate and the change in the slope means that the increment in effective velocity is higher than it would be expected if only the increment of pressure drop was considered. This behaviour is one of the most important consequences of cavitation and is due to the viscosity reduction in the zone occupied by the vapour phase along the orifice wall, which in turn reduces the friction losses in the channel. This finding has been experimentally and numerically analyzed in [27], where a strong reduction of the density was evidenced in the area occupied by the vapor phase as well as an important viscosity drop of around six hundred times with regard to the area occupied by pure liquid. This viscosity reduction led to more square velocity profiles and thus, to higher effective velocities.

If both nozzles are compared in terms of effective velocity, we have a different behaviour depending on the conditions (cavitating and non-cavitating). Indeed, if they are compared in non-cavitating conditions (backpressures higher than the critical value given in Table 3), due to the higher friction losses in VCO nozzle, the effective velocity is lower than that observed for the microsac nozzle. Nevertheless, for cavitating conditions, the differences in effective velocity are significantly reduced and, for the more severe cavitating conditions (160 MPa of injection pressure and low backpressures), the effective velocity can even be slightly higher in the VCO nozzles than in the microsac ones. The reason of this behaviour is, as already stated, due to the viscosity reduction in the zone occupied by the vapour phase along the orifice wall, which in turn reduces the friction losses along the orifice. This effect is more pronounced for VCO nozzles due to the higher intensity of cavitation observed, which makes a higher velocity increase with the pressure drop be expected.

4.1.3 Flow coefficients comparison at maximum needle lift.

Flow coefficients are useful to analyse the behaviour of the flow. The most important one is the discharge coefficient, C_d, defined as the mass flow divided by the maximum theoretical mass flow related to the maximum velocity of the flow given by Bernoulli's equation:

$$C_d = \frac{\dot{m}_f}{\rho_l A_o u_{th}} = \frac{\dot{m}_f}{A_o\sqrt{2\rho_l \Delta P}} \quad (22)$$

Where $\dot{m}_f$ is the mass flow, ΔP is the difference between the injection pressure (P_{in}) and the backpressure (P_b), $\Delta P = P_{in} - P_b$, A_o is the geometrical area of the outlet of the orifice and ρ_l is the liquid fuel density.

The second non-dimensional flow parameter is the velocity coefficient, C_v (Eq. (23)), which is defined as the effective velocity divided by the maximum Bernoulli´s theoretical velocity, u_{th} (Eq. (24)):

$$C_v = \frac{u_{eff}}{u_{th}} \tag{23}$$

$$u_{th} = \sqrt{\frac{2(P_{in} - P_b)}{\rho}} \tag{24}$$

The last non-dimensional flow parameter is the area coefficient, C_a (Eq. (25)), which is defined as the effective area (Eq. (23)) divided by the geometrical area.

$$C_a = \frac{A_{eff}}{A_0} \tag{25}$$

$$A_{eff} = \frac{{\dot{m}_f}^2}{\rho\, \dot{M}_f} \tag{26}$$

The 3 non-dimensional flow parameters are related, as shown in Eq. (27):

$$C_d = \frac{\dot{m}_f}{\rho_l\, A_o\, u_{th}} = \frac{\dot{M}_f}{\dot{m}_f\, u_{th}} \frac{{\dot{m}_f}^2}{\rho_l\, \dot{M}_f A_0} = C_v C_a \tag{27}$$

Fig. 5 displays the discharge coefficient, velocity coefficient and area coefficient for both nozzles and for the three injection pressures versus the square root of the pressure drop. In these graphs, two different zones can clearly be distinguished: a zone corresponding to non-cavitating conditions and a zone corresponding to cavitating conditions. The limit between both corresponds to the critical pressure drop (Table 3).

Regarding to the discharge coefficient, which is representative of the global losses in the nozzle, it shows a quite stable behaviour in the non-cavitating region, reaching maximum values of about 0.86 in the microsac nozzle and 0.8 for the VCO nozzle. This difference is consistent with the previous results of mass flow rate displayed in Fig. 4. In the cavitating zone, due to the mass flow collapse, the discharge coefficient experiences an abrupt drop. This drop starts at the point corresponding to the cavitation inception. It is remarkable that in the case of 160 MPa all the depicted points are cavitating for the VCO nozzle, whereas for the microsac nozzle there are two points (lower pressure drop) in non-cavitating conditions and the rest of points in cavitating conditions.

The aforementioned behaviour will have an impact on the effective area and effective velocity of injection, as it will be seen next.

The area coefficient also depicted in Fig. 5 takes values equal to one in non-cavitating conditions ([14][27]). Therefore, for these conditions, the velocity coefficient values equal the discharge coefficient ones. As happened for the discharge coefficient, the area coefficient drastically falls once cavitation phenomenon starts.

The velocity coefficient behaviour is in agreement with the results just analysed. Its value equals the discharge coefficient for non-cavitating conditions since the area coefficient equals the unity. As was previously observed in cavitating conditions, the effective velocity increases with the cavitation intensity. As can be seen in Fig. 5, for non-cavitating conditions the velocity coefficient is higher for the microsac nozzle, but the differences between them are reduced with cavitation intensity.

Indeed, in the case of 160 MPa and for low backpressures (higher pressure drop), higher values for the VCO nozzle can be observed due to its higher cavitation intensity level.

4.1.4 Streamlines and cavitation morphology

In Fig. 6, the appearance of the cavitation in both kinds of nozzles is shown, together with the streamlines followed by the fluid particles. That representation corresponds to the injection pressure of 160 MPa, discharge pressure of 3 MPa and maximum needle lift. As it can be seen in the upper part of the figure, for the VCO nozzle the cavitation is originated at the upper corner of the orifice inlet, where the streamlines suffer a pronounced deflection when the fluid enters the orifice. In that zone, as it is observed in the streamlines of the left side at the bottom of the figure, there is a detachment of the flow that leads to a recirculation region (in the figure, the zone of the orifice not swept by the streamlines) with an important local acceleration, where the pressure decreases dramatically as a consequence, thus leading to cavitation.

In the case of the microsac nozzle, the cavitation is not only originated at the upper corner of the orifice inlet but also at the lower inlet corner. In this case, as the right side at the bottom of the figure shows, the deflection suffered by the flow is less important, since the higher value available between the needle wall and the inner nozzle wall facilitates the fluid entrance. This would explain the lower susceptibility of this nozzle to cavitate. However, part of the flow that enters the orifice in this case comes from the sac, which originates a small recirculation region at the lower corner of the orifice inlet leading to cavitation, though less intense.

Anyway, as it has been noted in the analysis of the critical pressure conditions that lead to cavitation in one nozzle and the another, the cavitation intensity is higher in the VCO nozzle (since it starts cavitating earlier) than in the microsac nozzle. This result is reflected in the vapour phase fraction in the middle section of the orifice of both nozzles shown in Fig. 6, although similar conclusions could be extracted if any other section of the orifice had been compared, including the nozzle outlet.

4.2 Partial needle lifts

In this section, an extension of the results analysed for maximum needle lift conditions (250 µm) is made to different partial needle lifts of 50, 75, 100, 150 and 200 µm. In Fig. 7, the results of mass flow are shown for both nozzles and the three injection pressures. Although the behaviour that the nozzles exhibit for each of the needle lifts is the same as described in Section 4.1.1 with regard to the mass flow collapse, there is a fundamental difference concerning the scaling of the results with the different needle lifts: in the case of the VCO nozzle, the increase in needle lift always leads to an increase in its mass flow, i.e. the needle lift strongly influences the results. In the microsac nozzle, however, there is a needle lift among 50 and 75 µm from which the needle stops having an influence on the mass flow. For this reason, the differences among both nozzles when compared at low or medium needle lift may be way more important than those previously observed at maximum needle lift. This result is very important taking into account that the injection process in current diesel engines is heavily controlled by the needle opening and closing transient stages, due to the usage of multiple injections of low entity (in the case of pilot and post-injections) in order to mitigate emissions ([37][38]).

There are two reasons to justify the fact that the needle does not have influence from 75 µm for the microsac nozzle. Firstly, the critical section which determines the flow behaviour from 75 µm is the orifice inlet instead of the needle closing as it was for lower needle lifts. Secondly, from that needle position the path followed by the fluid to enter in the orifice remains invariable. This second phenomenon occurs later in the VCO nozzle and thus, a continuous increase of the mass flow can be seen as the needle moves upward.

The same conclusion is reached when the momentum flux and effective velocity are compared (Figs. 8 and 9, respectively). There is a sharp dependency of the VCO nozzle results on the needle lift, whereas they are independent of the needle lift for the microsac nozzle from a relatively small needle lift (50-75 µm). As it was the case for the mass flow, the differences in effective velocity between both nozzles become much more noticeable when compared at a small needle lift than in the case of maximum needle lift. Bearing in mind that the injection velocity plays a key role in the fuel-air mixing process ([3][15][36]), this fact may act against the VCO nozzles in the transient stages of needle opening and closing, which may occupy an important percentage of the injection time.

Figs. 10, 11 and 12 show the same results in non-dimensional terms, making use of the flow coefficients, which were used in section 4.1.3. for the description of the flow at maximum needle lift.

The discharge coefficients depicted in Figure 10 show lower values for low needle lifts due to the losses located at the needle closing in the microsac nozzle and at the orifice entrance in the VCO nozzle. For high needle lifts, the discharge coefficient keeps constant for both types of nozzles while there is no vapour phase, changing its behavior when cavitation phenomenon develops. This change occurs both at high lifts from critical cavitation conditions and at low needle lifts due to the presence of vapour in the needle closing and/or the orifice depending on the type of nozzle. This drop of the discharge coefficient is justified by the mass flow collapse seen in Figure 7.

As far as the velocity coefficient is concerned, plotted in Figure 11, at high needle lifts the coefficient keeps constant at non cavitating conditions and increases with the reduction of the backpressure once cavitation starts to develop in the orifice. For lower needle lifts, such as 50 µm for the microsac nozzle or 50 and 75 μm for the VCO nozzle, only the presence of vapour bubbles inside the nozzle orifice (in its upper or lower part) induces to a velocity coefficient rise.

Furthermore, that presence of vapour bubbles in the nozzle orifice is the reason for the area coefficient drop seen in Figure 12 for all the needle lifts simulated. As seen previously at maximum needle lift, this coefficient remains always constant with values near to 1 as long as there is no vapour in the orifice. However, if the pressure difference between the injection and the discharge is big enough to produce cavitation in the orifice, the area coefficient decreases as a consequence of the reduction of the liquid phase effective area.

5. CONCLUSIONS

In the present paper a computational study about the differences in the internal flow between a VCO nozzle and a microsac nozzle has been carried out by using a Homogeneous Equilibrium Model validated previously and also in this study. For this research, six needle lifts and 3 injection pressures have been deeply studied with a backpressure sweep in order to simulate both cavitating and non-cavitating conditions. The main conclusions are summarized in the following points.

The study of the flow in stationary conditions of maximum needle lift has led to the following conclusions:

- The VCO nozzle features higher losses, which is noticed from the lower mass flow for a given pressure condition. These higher losses are justified by the higher deflection suffered by the streamlines at the orifice entrance, thus providing a lower mass flow and leading to a lower discharge coefficient than the microsac nozzle.

- The higher deflection suffered by the fluid particles when facing the entrance to the orifice in the VCO nozzle as opposed to the microsac nozzle leads to the inception of cavitation taking place for conditions of lower pressure difference, i.e. at higher discharge pressures. thus, this kind of nozzles is more prone to cavitate than the microsac nozzles.

- The two aforementioned conclusions are in line with the experimental evidences found in the literature. These evidences refer to the higher discharge coefficient found for the microsac nozzle and specially to the higher spreading angle for the VCO nozzle. Keeping in mind that the VCO nozzle is more prone to cavitate than the microsac nozzle, and considering than one of the main effects of cavitation is the increase of the spray spreading angle due to the higher turbulence generated on the flow ([15][27]), these results would be compatible with the results herein shown.

- The VCO nozzle exhibits, in general, lower values of momentum flux and effective injection velocity. However, under conditions in which the cavitation becomes more intense (higher pressure differences above the critical one), the differences get smaller. Under extremely cavitating conditions (high injection pressure and very low backpressure) the situation may be reverted due to the increase that the cavitation itself produces on the injection velocity.

From the generalization of the study to partial needle lifts, the following conclusions are reached:

- A higher sensitivity of the results with the needle lift has been noted in the case of the VCO nozzle from the comparison of both nozzles at different partial needle lifts lower than the maximum one. The results for this nozzle are strongly affected by the presence of the needle. However, in the case of the microsac nozzle, there is a small needle lift (among 50 and 75 µm) for which the needle stops influencing the results, which experience very small variations from that value.

- As a consequence of the previous observation, the differences observed for both nozzles at maximum needle lift are highly amplified when considering small needle lifts.

ACKNOWLEDGEMENTS

This work was partly sponsored by “Ministerio de Economía y Competitividad” in the frame of the project “Comprensión de la influencia de combustibles no convencionales en el proceso de inyección y combustión tipo diesel”, Reference TRA2012-36932. This support is gratefully acknowledged by the authors.

The authors would like to thank the computer resources, technical expertise and assistance provided by the Universidad de Valencia in the use of the supercomputer “Tirant”.

REFERENCES

[1] C.A.S. Hall, J.G. Lambert, S.B. Balogh, EROI of different fuels and the implications for society, Energy Policy 64 (2014), pp. 141–152.

[2] A. Zecca, L. Chiari, Fossil-fuel constraints on global warming, Energy Policy 38 (2010), pp.1–3.

[3] J.B. Heywood. Internal combustion engine fundamentals. McGraw-Hill Publishing; 1988, ISBN 007028637X.

[4] R. Payri., F.J. Salvador, J. Gimeno, V. Soare, Determination of diesel spray characteristics in real engine in-cylinder aire density and pressure conditions, Journal of mechanical science and technology, 19 (2005), pp. 2040-2052.

[5] R. Payri., F.J. Salvador, J. Gimeno, L.D. Zapata, Diesel nozzle geometry influence on spray liquid-phase fuel penetration in evaporative conditions, Fuel, 87 (2007), pp. 1165-1176.

[6] R. Payri, F.J. Salvador, J. Gimeno, J. de la Morena, Effects of nozzle geometry on direct injection diesel engine combustion process, Applied thermal engineering, 29 (2009), pp. 2051-2060.

[7] R. Payri, F.J. Salvador, J. Gimeno, J. de la Morena, Influence of Injector technology on injection and combustion development-Part 2: combustion analysis, Applied Energy, 88 (2011), pp. 1130-1139.

[8] Z.Y. Sun, G.X. Li, C. Chen, Y.S. Yu, G.X. Gao, Numerical investigation on effects of nozzle's geometric parameters on the flow and the cavitation characteristics within injector's

nozzle for a high-pressure common-rail DI diesel engine, Energy Conversion and Management 89 (2015), 843-861.

[9] LM. Rodriguez-Anton, J. Casanova-Kindelan, G. Tardajos, High pressure physical properties of fluids used in diesel injection Systems, SAE paper 2000-01-2046;2000.

[10] R. Payri, F.J. Salvador, J. Gimeno, G. Bracho, The effect of temperature and pressure on thermodynamic properties of dieseland biodiesel fuels, Fuel 90 (2011) 1172–1180.

[11] X. Wang, Z. Huang, W. Zhang, O.-A. Kuti, K. Nishida, Effects of ultra-high injection pressure and micro-hole nozzle on flame structure and soot formation of impinging diesel spray, Fuel 90 (2011) 1172–1180.

[12] S. Som, A.I. Ramirez, D.E. Longman, S.K. Aggarwal, Effect of nozzle orifice geometry on spray, combustion, and emission characteristics under diesel engine conditions, Fuel 90 (2011) 1267–1276.

[13] C. Sayin, M. Gumus, M. Canakcim, Influence of injector hole number on the performance and emissions of a DI diesel engine fueled with biodiesel-diesel fuel blends, Applied Thermal Engineering 61 (2013) 121-128.

[14] F.J. Salvador, J. Martínez-López, M. Caballer, C. De Alfonso, Study of the influence of the needle lift on the internal flow and cavitation phenomenon in diesel injector nozzles by CFD using RANS methods, Energy Conversion and Management 66 (2013) 246–256.

[15] F. Payri, V. Bermúdez, R. Payri, F.J. Salvador, The influence of cavitation on the internal flow and the spray characteristics in diesel injection nozzles, Fuel 83 (2004) pp. 419-431

[16] C. Bae, J. Kang, Diesel spray development of VCO nozzles for high pressure direct-injection, SAE Technical Paper 2000-01-1254, 2000, doi:10.4271/2000-01-1254.

[17] Y. Takeda, N. Ishikawa, M. Komori, K. Tsujimura, Diesel combustion improvement and emissions reduction using VCO Nozzles with high pressure fuel injection, SAE Technical Paper 940899, 1994, doi:10.4271/940899.

[18] M. Kubo, T. Araki, S. Kimura, Internal flow analysis of nozzles for DI diesel engines using a cavitation model, JSAE Review, Volume 24, Issue 3, July 2003, Pages 255-261

[19] M., Sjöberg, H., Ångström, D.Konstanzer, O. Thorin, The rotating injector, a new system for diesel combustion, SAE Technical Paper 982678, 1998, doi:10.4271/982678.

[20] S. Molina, F.J. Salvador, M. Carreres, D. Jaramillo, A computational investigation on the influence of the use of elliptical orifices on the inner nozzle flow and cavitation development in diesel injector nozzles, Energy Conversion and Management 79 (2014), 114-127.

[21] V. Bermúdez, R. Payri, F.J. Salvador, Study of the influence of nozzle seat type on injection rate and spray behaviour, Proceedings of the institution of mechanical engineers Part-D, Journal of automobile engineering, 219 issue D5 (2005), pp. 677-689.

[22] H. Roth, , M. Gavaises, C. Arcoumanis, Cavitation initiation, its development and link with flow turbulence in diesel injector nozzles, SAE Technical Paper 2002-01-0214, doi:10.4271/2002-01-0214

[23] C. Soteriou, R. Andrews, M. Smith, Further studies of cavitation and atomization in diesel injection. SAE Paper 1999-01-1486.

[24] OpenFOAM® is a registered trade mark of OpenCFD Limited http://www.opencfd.co.uk/openfoam/index.html

[25] F.J. Salvador, S. Hoyas, R. Novella, J. Martínez-López, Numerical simulation and extended validation of two-phase compressible flow in diesel injector nozzles, Proceedings of the institution of mechanical engineers part-D-Journal of automobile engineering, vol. 225, (2011), pp. 545-563.

[26] F.J. Salvador, J.-V. Romero, M.-D. Roselló, J. Martínez-López. Validation of a code for modeling cavitation phenomena in Diesel injector nozzles. Mathematical and Computer Modelling 52 (2010), 1123-1132.

[27] F. Payri, R. Payri, F.J. Salvador, J. Martínez-López, A contribution to the understanding of cavitation effects in diesel injector nozzles through a combined experimental and computational investigation, Computer and Fluids, 58 (2012), pp. 88-101.

[28] F.J. Salvador, J. Martínez-López, J.-V. Romero, M.-D. Roselló, Computational study of the cavitation phenomenon and its interaction with the turbulence developed in diesel injector nozzles by Large Eddy Simulation (LES), Mathematical and Computer Modelling, 57 (2013), pp. 1656-1662.

[29] T.J. Chung, Computational Fluid Dynamics, second edition, Cambridge University Press (2010) ISBN 978-0-521-76969-3.

[30] H.B. Stewart, Two-phase flow: models and methods, J. Comput. Phys., vol. 56 (1984), pp. 363-409.

[31] V. Yakhot, S.A. Orszag, S. Thangam, T.B. Gatski, C.G. Speziale, Development of turbulence models for shear flows by a double expansion technique, Phys. Fluids A 4 (1992), 1510.

[32] V. Macián, R. Payri, X. Margot, F.J. Salvador, A CFD analysis of the influence of diesel nozzle geometry on the inception of cavitation, Atomization and sprays, vol. 13 (2003), pp. 579-604.

[33] Tirant Node, http://www.bsc.es/annual-report/2009/wikiar.bsc.es/index.php5/Universidad_de_Valencia_-_Tirant_Node.html

[34] F.P. Kärrholm. Numerical Modelling of Diesel Spray Injection, Turbulence Interaction and Combustion, PhD. Thesis, Chalmers University of Technology, 2008

[35] J.M. Desantes, R. Payri, J.M. García, F.J. Salvador, A contribution to the understanding of isothermal diesel spray dynamics, Fuel, 86 (2007), pp. 1093-110.

[36] J.M. Desantes, F.J. Salvador, J.J. López, J. de la Morena, Study of mass and momentum transfer in diesel sprays based on a theoretical derivation, Experiments in fluids, vol. 50 (2) (2011), pp. 236-246.

[37] R. Payri, F.J. Salvador, P. Martí-Aldaraví, J. Martínez-López, Using one-dimensional modeling to analyse the influence of the use of biodiesels on the dynamic

behavior of solenoid-operated injectors in common rail systems: Detailed injection system model, Energy Conversion and Management 54 (2012), pp.90–99.

[38] F.J. Salvador, J. Gimeno, J. de la Morena, M. Carreres, Using one-dimensional modeling to analyse the influence of the use of biodiesels on the dynamic behavior of solenoid-operated injectors in common rail systems: Results of the simulations and discussion, Energy Conversion and Management 54 (2012), pp. 122-132.

List of Tables:

List of Figures:

Nozzle	***Di* [μm]**	***Do* [μm]**	***r* [μm]**	***r/Do* [-]**	***L/Do* [-]**	***Nozzle Angle (θ)[º]***
6-hole	170	170	30	0.074	5.71	72.5

Table 1: Nozzle´s geometrical characteristics.

Injection Pressure [MPa]	***Backpressure [MPa]***	
30	microsac	3,5,7,9,10,15,20
	VCO	
80	microsac	3,5,7,9,10,20,30,40,50
	VCO	
160	microsac	3,5,7,9,10,20,30,40,50
	VCO	3,5,7,9,10,20,30,40,50,60,70,80,90,100,110

Table 2: Boundary conditions.

	Critical cavitation conditions in terms of backpressure values needed for inducing cavitation inception in MPa.	
Injection Pressure [MPa]	VCO	microsac
30	9.5	7
80	25	18
160	50	36

Table 3: Critical cavitation conditions at maximum needle lift (250μm).

	Critical Cavitation Number- K_{crit}	
Injection Pressure [MPa]	VCO	microsac
30	1.46	1.3
80	1.45	1.29
160	1.44	1.29

Table 4: Critical Cavitation Number (K_{crit}) at maximum needle lift (250μm).

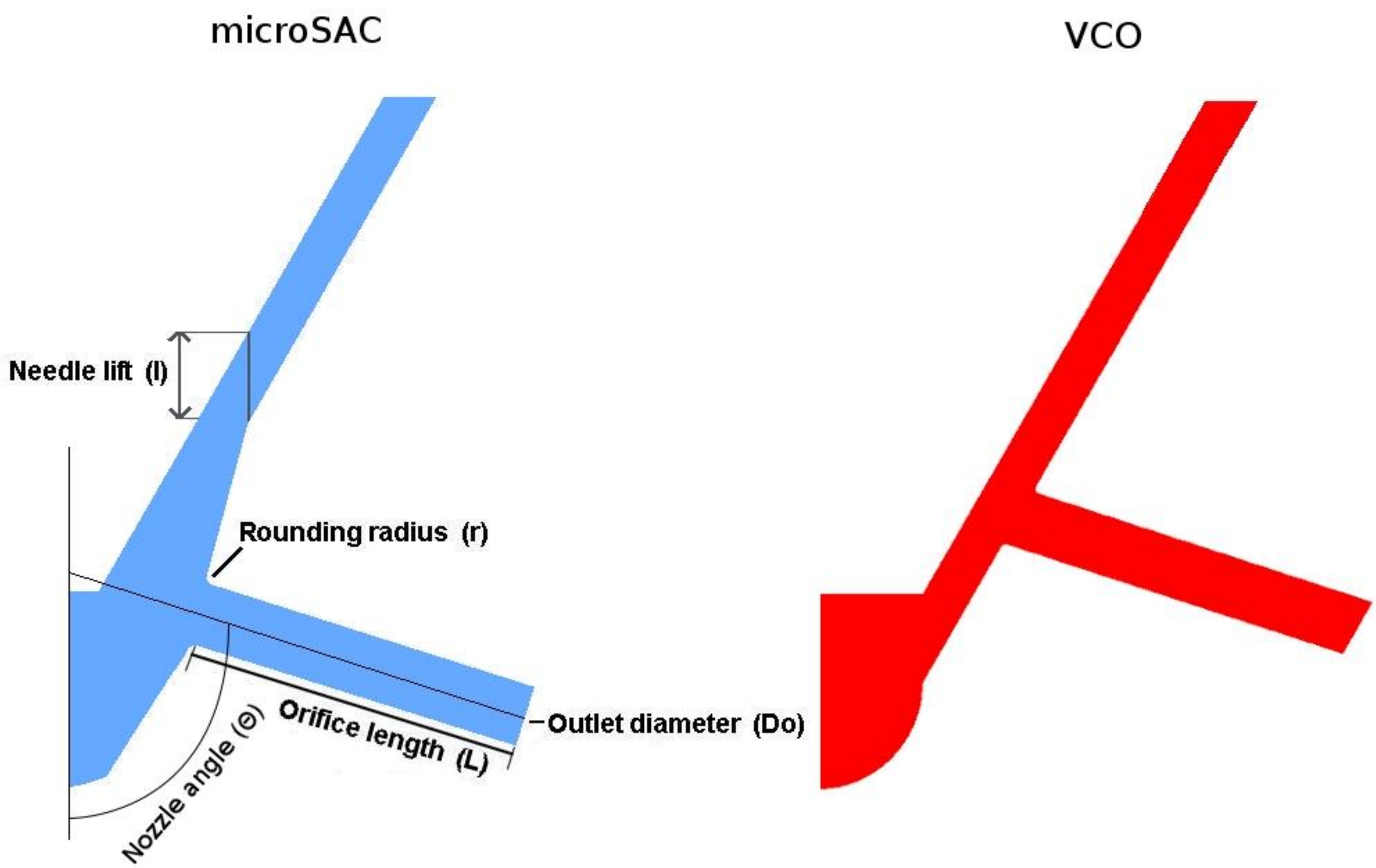

Fig. 1: Nozzle's geometrical parameters.

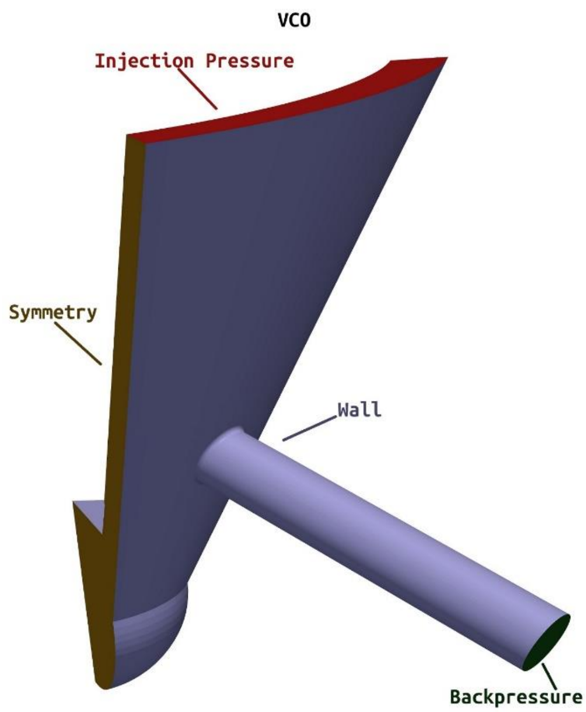

Fig. 2: Boundary conditions.

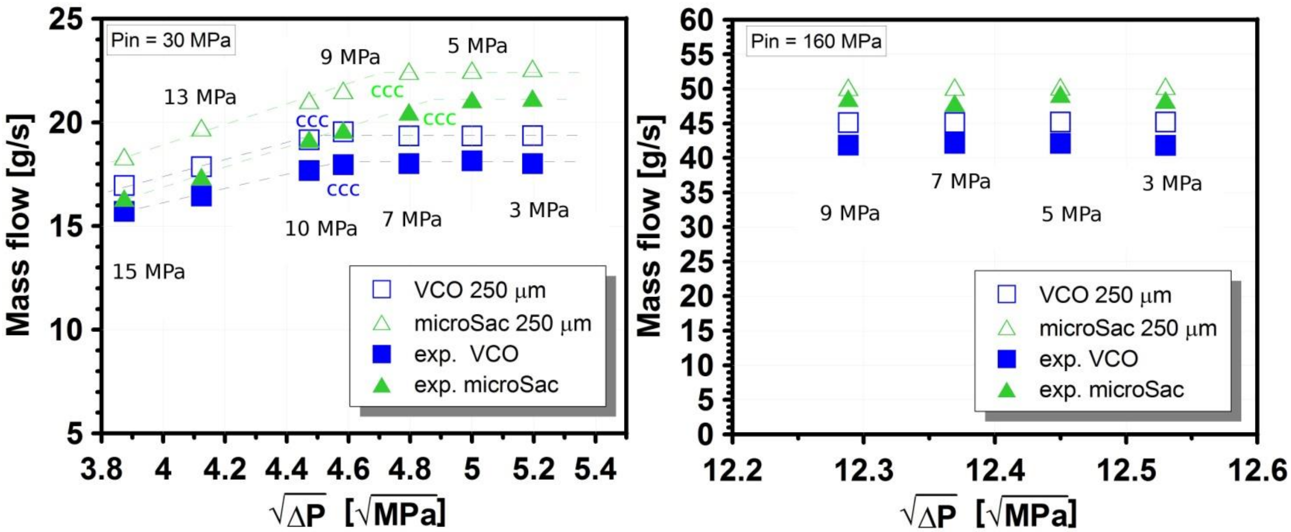

Fig. 3: Model validation using mass flow rate measurements.

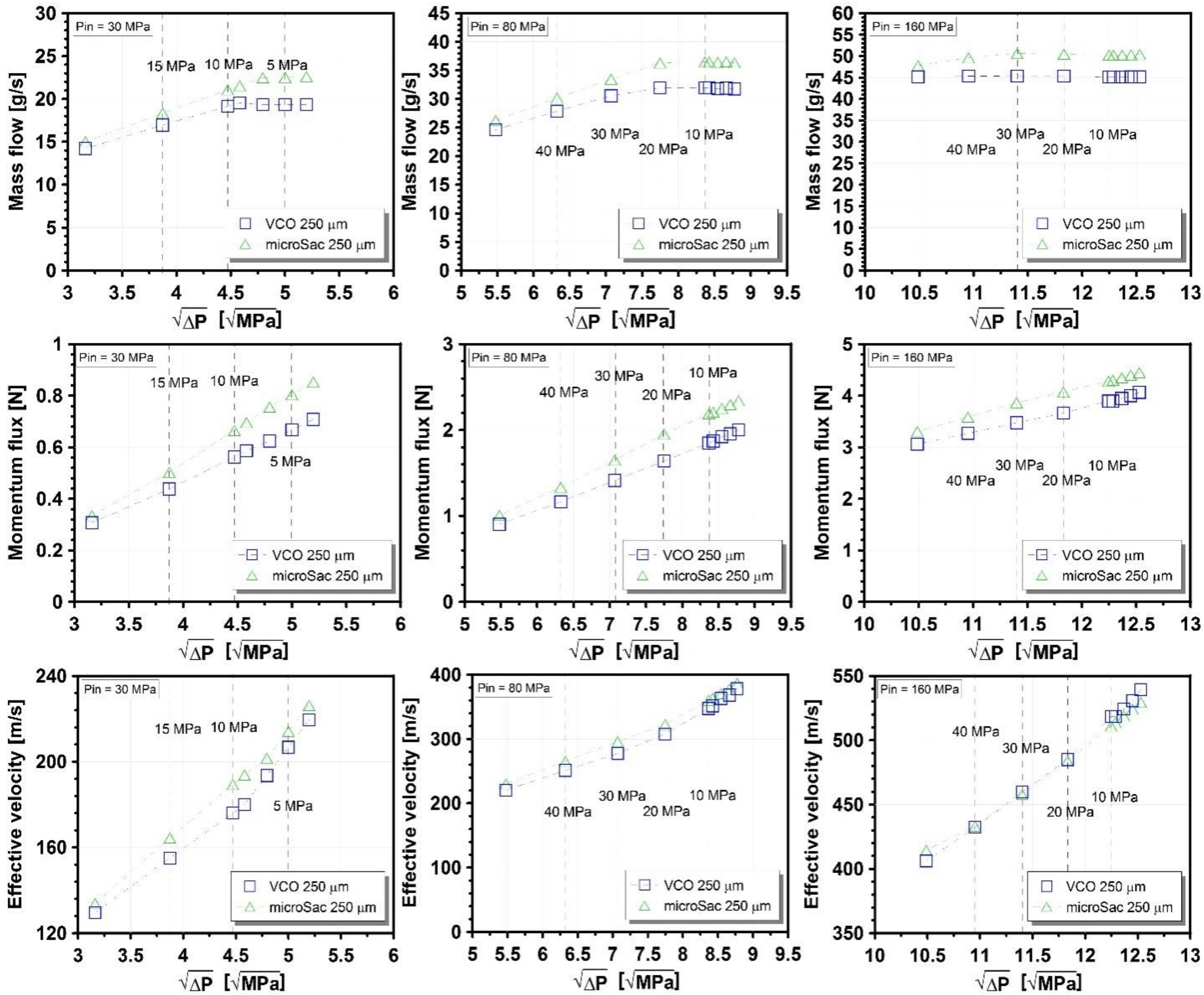

Fig. 4: Results of mass flow, momentum flux and velocity at maximum needle lift.

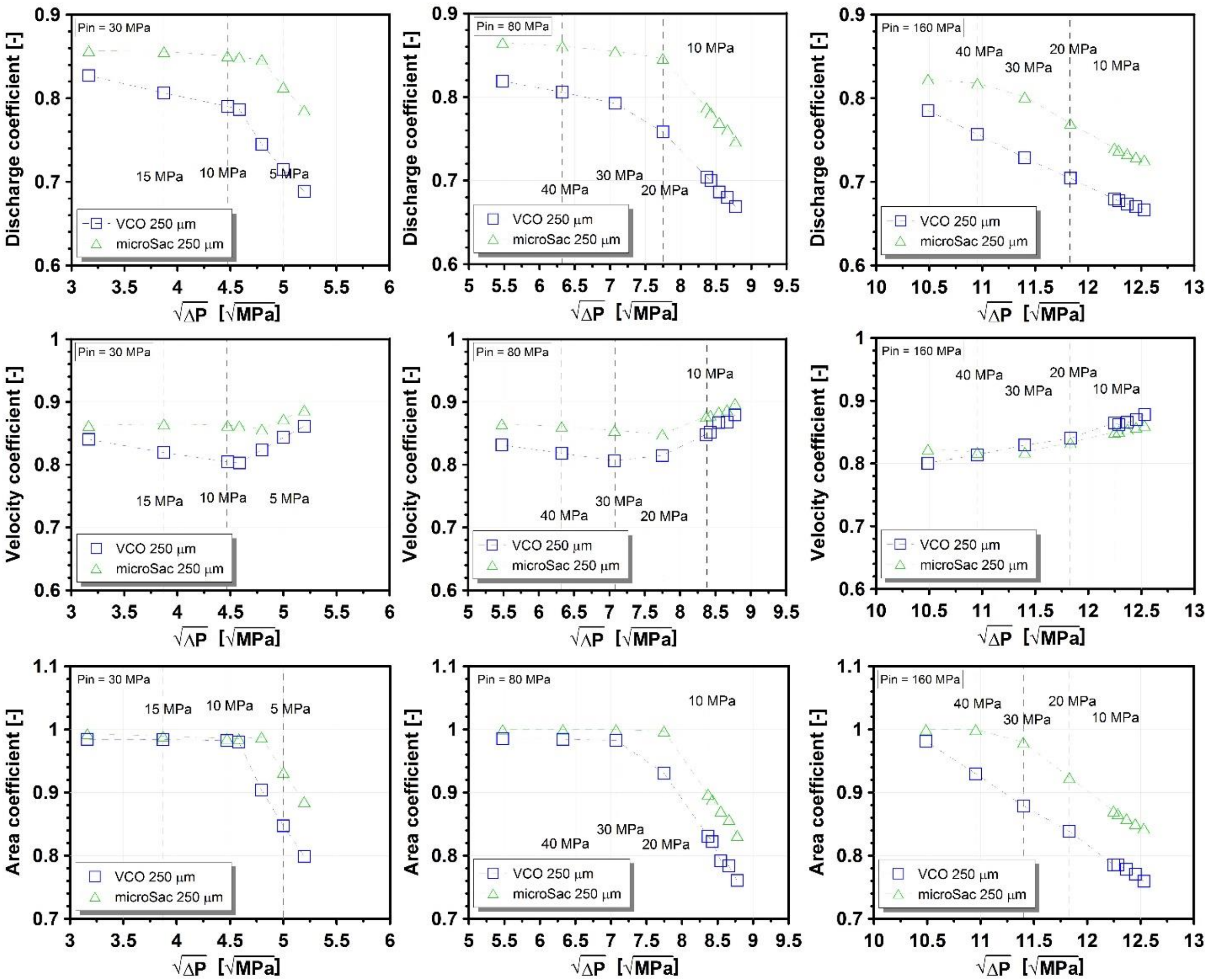

Fig. 5: Flow coefficients at maximum needle lift.

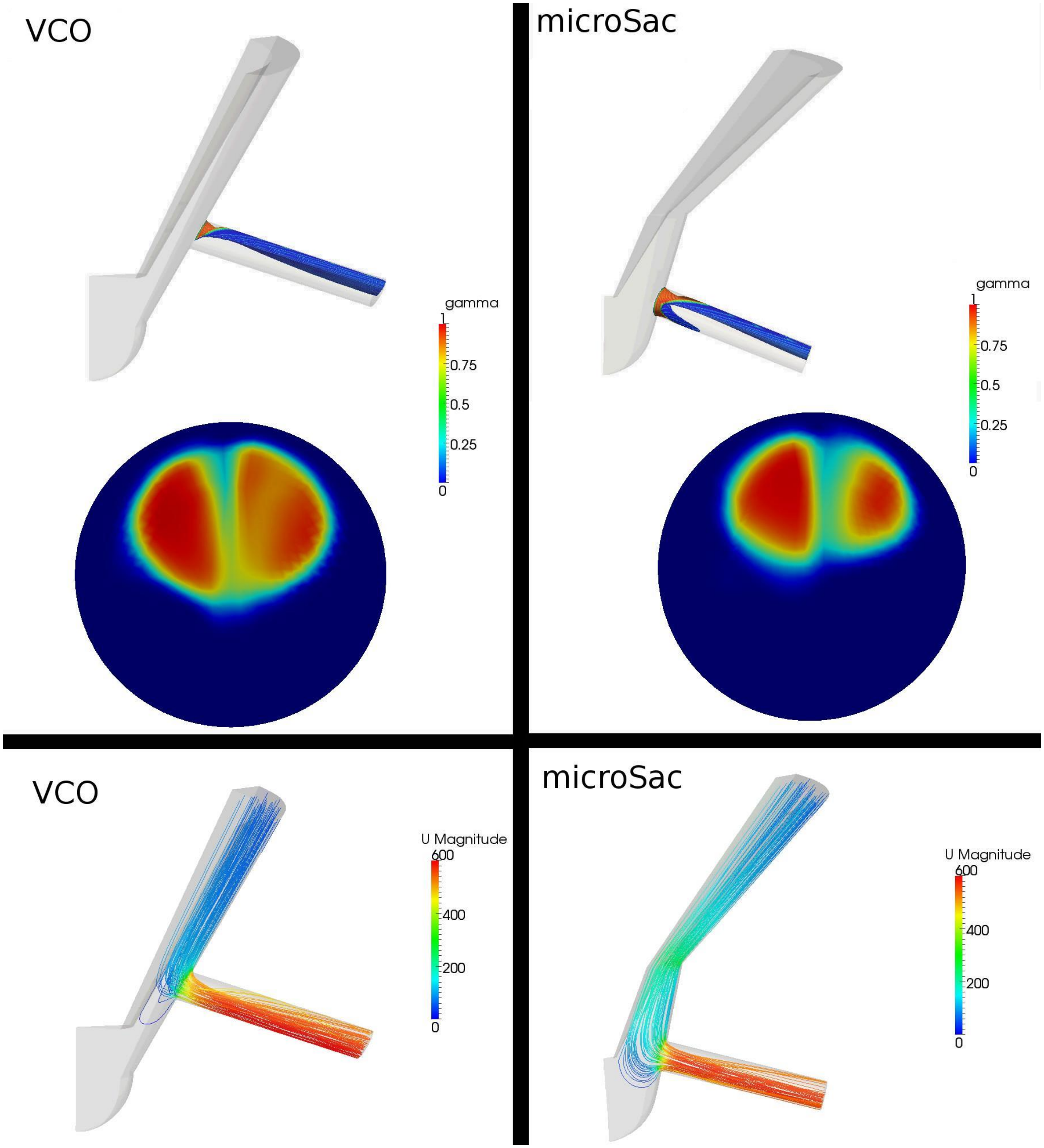

Fig. 6: Cavitation morphology, vapour phase fraction in a middle section of the orifice and streamlines at maximum needle lift conditions for Pin=160 MPa - Pb=3 MPa.

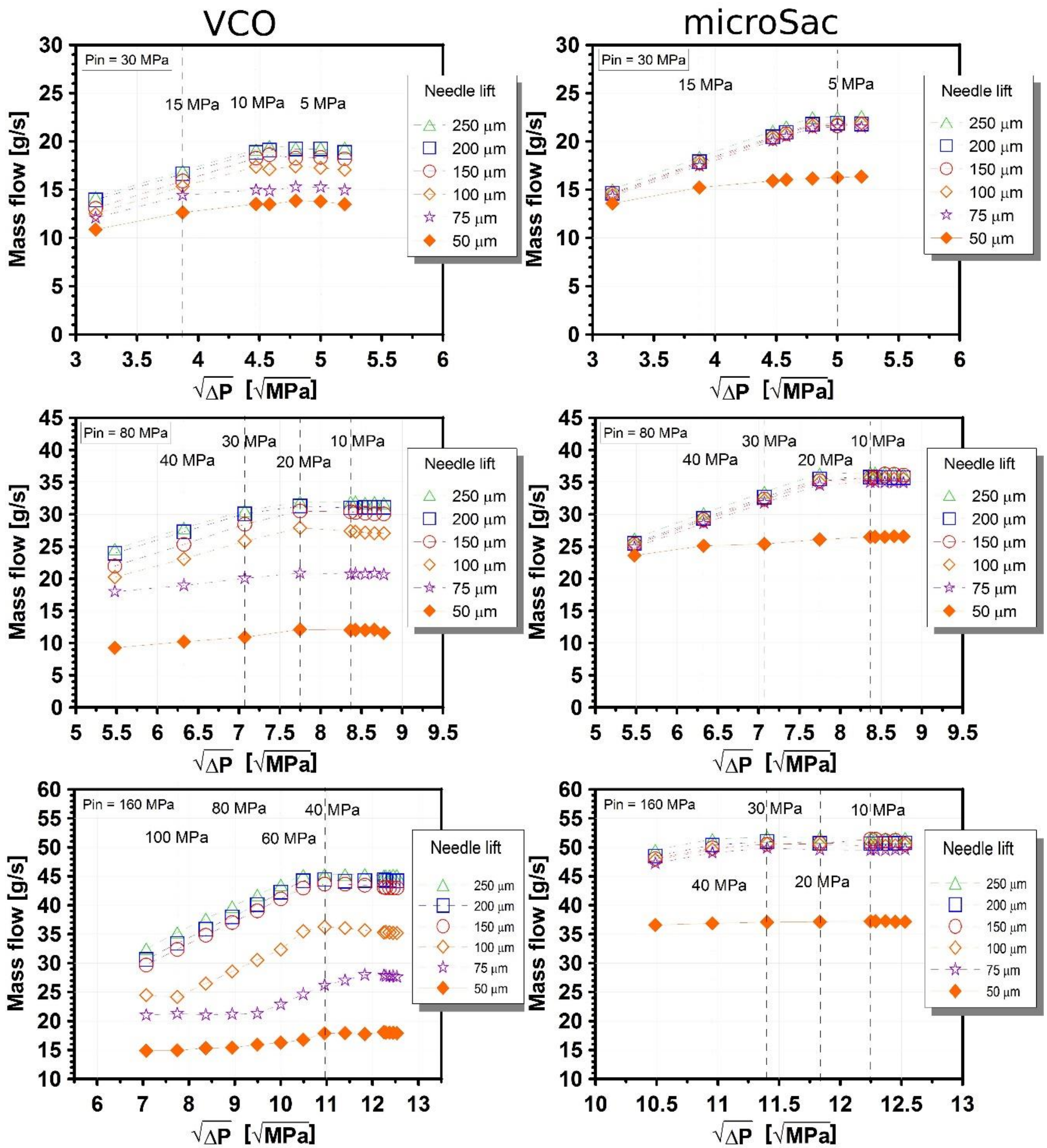

Fig. 7: Mass flow for all needle lifts.

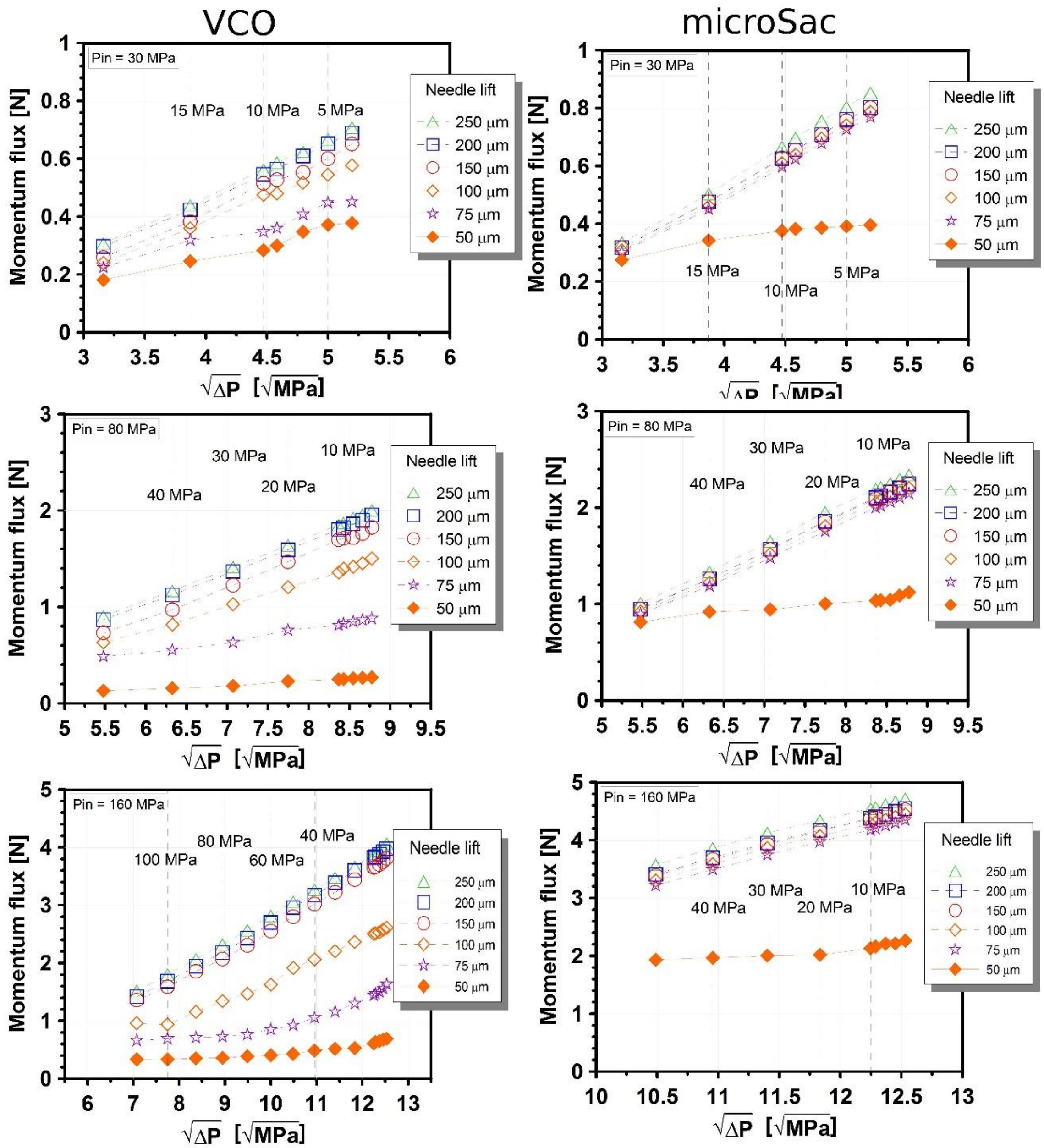

Fig. 8: Momentum flux for all needle lifts.

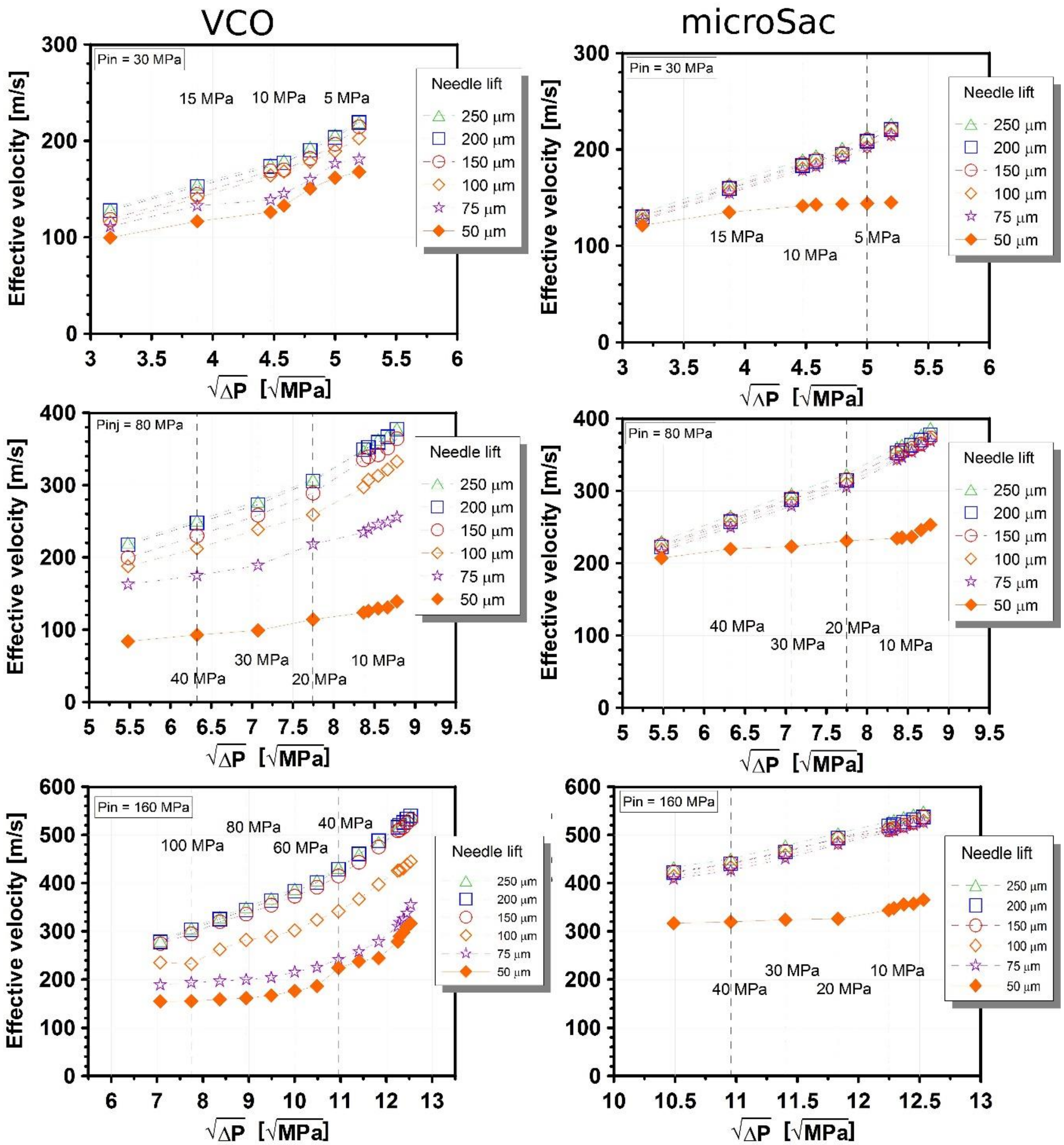

Fig. 9: Effective velocity for all needle lifts.

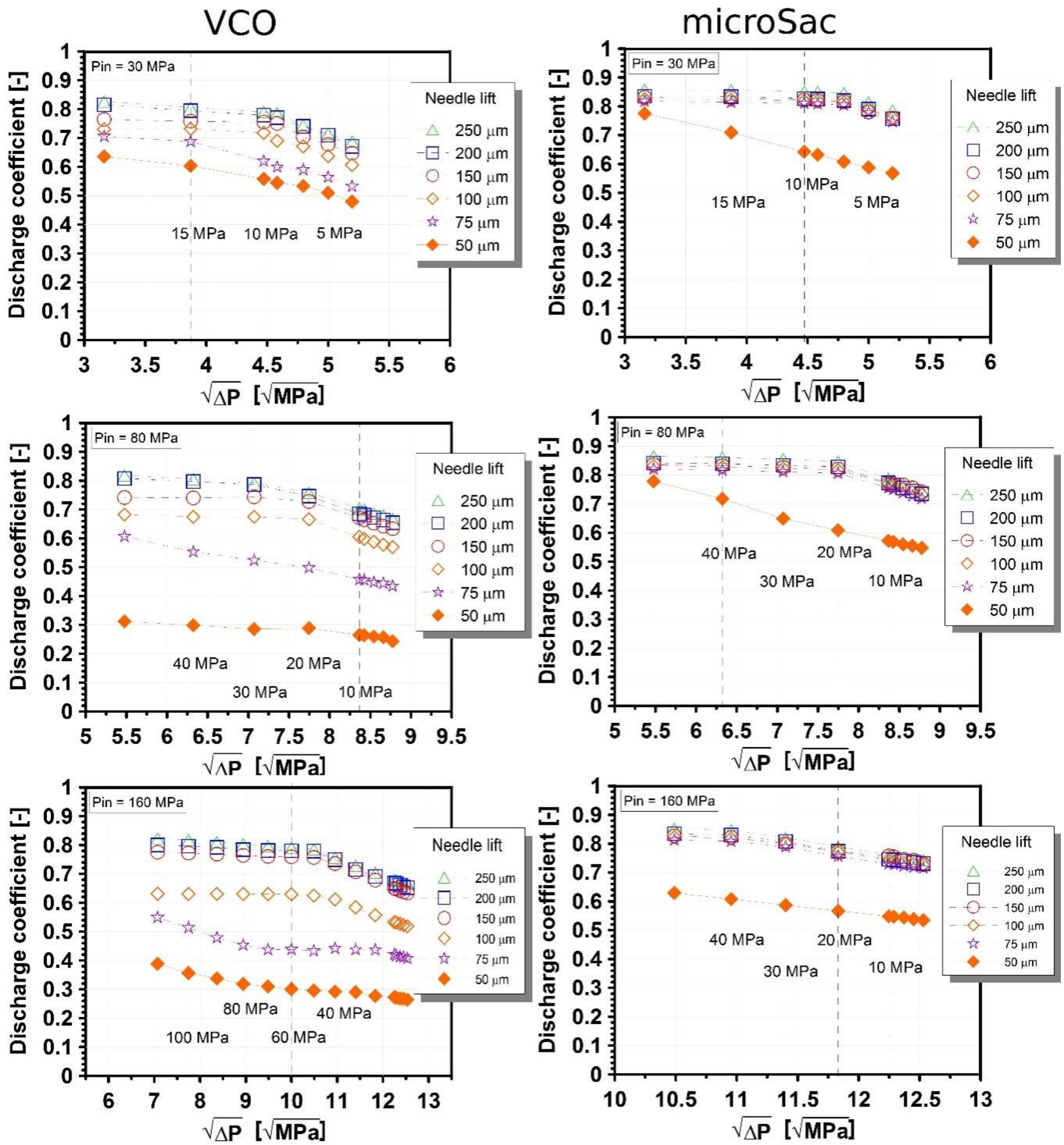

Fig. 10: Discharge coefficient for all needle lifts.

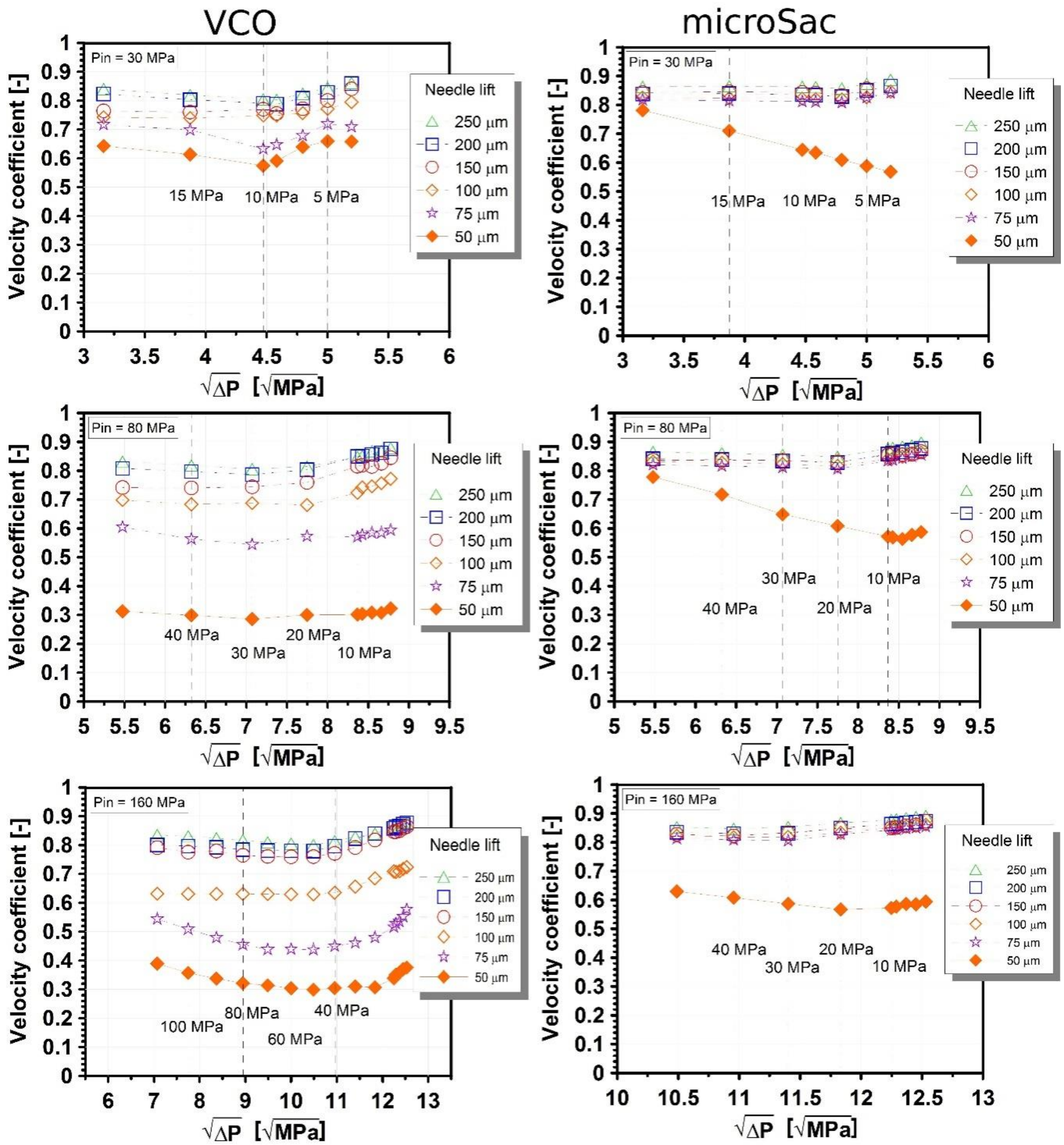

Fig. 11: Velocity coefficient for all needle lifts.

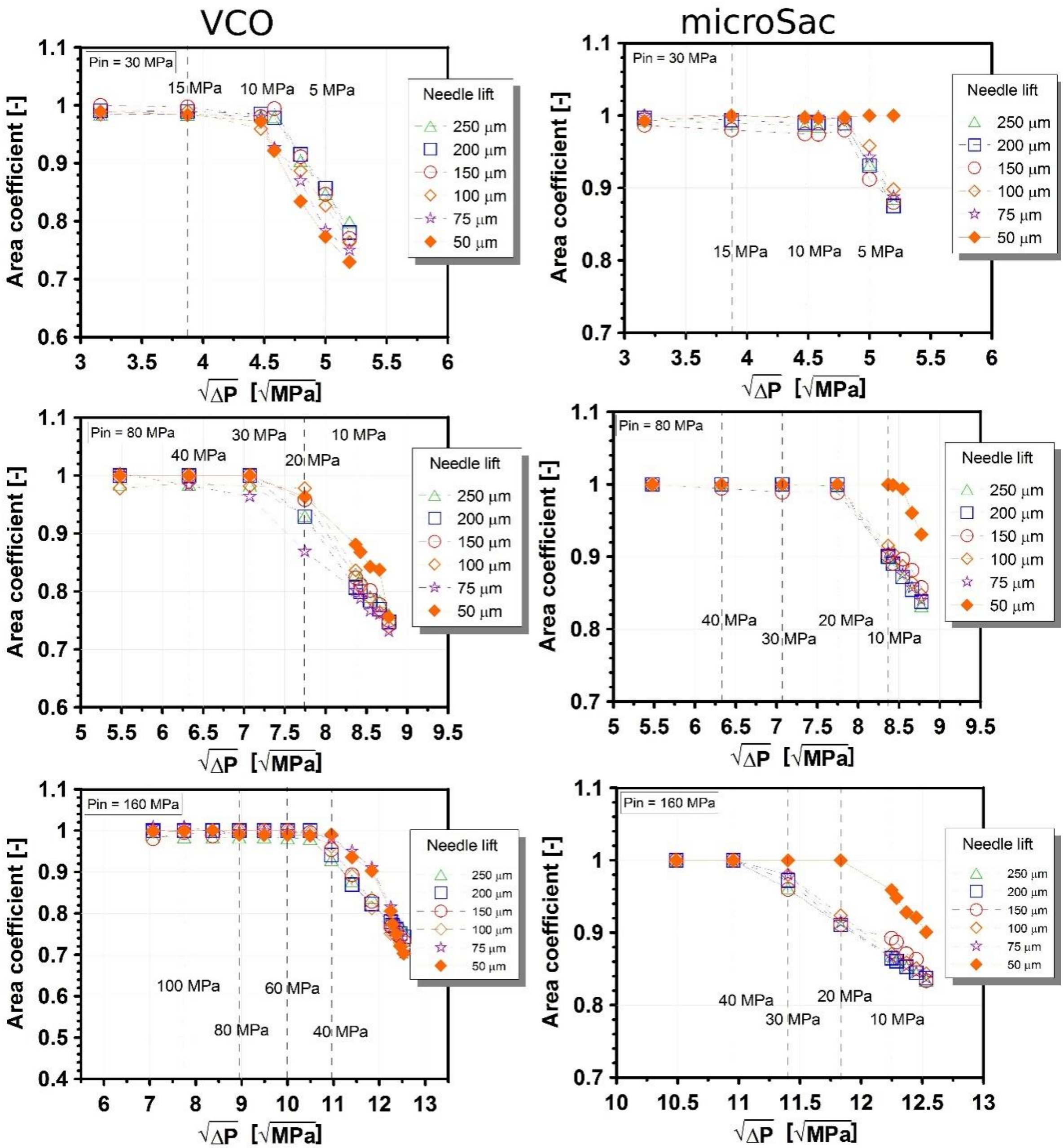

Fig. 12: Area coefficient for all needle lifts.